



## Experimental determination of atomic alignment of $_{42}\text{Mo}$ , $_{48}\text{Cd}$ , and $_{49}\text{In}$ with differential x-ray intensity ratios by 100–250-keV proton impact

Xing Wang ,\* Xuan Liu , Zhongfeng Xu, Jieru Ren, and Yongtao Zhao

Ministry of Education Key Laboratory for Nonequilibrium Synthesis and Modulation of Condensed Matter,  
 Shaanxi Province Key Laboratory of Quantum Information and Quantum Optoelectronic Devices,  
 School of Physics, Xi'an Jiaotong University, Xi'an 710049, China

Rui Cheng, Yu Lei, and Yanhong Chen

Institute of Modern Physics, Chinese Academy of Sciences, Lanzhou 730000, China

Yu Liu, Xianming Zhou, and Xiaohan Zhang

Ion Beam and Optical Physical Laboratory, Xianyang Normal University, 712000 Xianyang, China



(Received 23 December 2021; revised 9 March 2022; accepted 3 May 2022; published 13 May 2022)

This work aims to study the alignment properties of electron vacancies produced by proton bombardment in the low-energy region from 100 to 250 keV. The alignment parameter  $\mathcal{A}_{20}$  of  $_{42}\text{Mo}$ ,  $_{48}\text{Cd}$ , and  $_{49}\text{In}$  ions after  $L_3$  subshell ionization has been investigated experimentally. The typical  $L$  x-ray spectra are measured for each target at emission angles from  $115^\circ$  to  $155^\circ$ . The angular dependence of differential intensity ratios  $L_\alpha/L_{\beta_1}$  and  $L_{\beta_2}/L_{\beta_1}$  is studied as a function of the second-order Legendre polynomial  $P_2(\cos\theta)$ . Our result demonstrates that  $L_\alpha$  and  $L_{\beta_2}$  lines exhibit anisotropic emission spatially. The anisotropy parameter is converted to the alignment parameter by considering the Coster-Kronig (CK) correction coefficient and anisotropy coefficient. The results are compared with theoretical prediction within the framework of the semiclassical theory of inner-shell ionization, and good agreement is found in general. A small discrepancy around the inflection point of the alignment parameter is attributed to the atomic parameters employed only for single ionization in the CK correction coefficient.

DOI: [10.1103/PhysRevA.105.052807](https://doi.org/10.1103/PhysRevA.105.052807)

### I. INTRODUCTION

The characteristic radiation of atoms is utilized extensively in atomic physics and plasma physics [1–3]. As demonstrated by Berezhko *et al.* [4,5] and Jitschin *et al.* [6,7], fluorescent radiation emitted in the decay of a vacancy with total angular momentum  $j > 1/2$  can generally have an anisotropic distribution. For the  $L_3$  subshell ( $j = 3/2$ ), the magnitude of the alignment parameter  $\mathcal{A}_{20}$  can be quantified as the relative difference in the ionization cross sections  $\sigma(j, m_j)$  related to the magnetic quantum numbers  $m_j = 3/2$  and  $m_j = 1/2$  and is written as

$$\mathcal{A}_{20} = \frac{\sigma\left(\frac{3}{2}, \frac{3}{2}\right) - \sigma\left(\frac{3}{2}, \frac{1}{2}\right)}{\sigma\left(\frac{3}{2}, \frac{3}{2}\right) + \sigma\left(\frac{3}{2}, \frac{1}{2}\right)}. \quad (1)$$

Experimentally, the alignment parameter  $\mathcal{A}_{20}$  can be established by the measurement of the angular distribution of Auger electrons or characteristic x rays in the subsequent deexcitation of singly ionized atoms [8–12]. In terms of the dipole approximation, the differential intensity  $dI(\theta)$  at emission angle  $\theta$  relative to the incident beam direction is

given by [4]

$$\begin{aligned} \frac{dI(\theta)}{d\Omega} &= \frac{I_{\text{tot},i}}{4\pi} [1 + \beta P_2(\cos\theta)] \\ &= \frac{I_{\text{tot},i}}{4\pi} [1 + \alpha\kappa\mathcal{A}_{20}P_2(\cos\theta)], \end{aligned} \quad (2)$$

where  $\Omega$  is the solid angle subtended to the target in the experimental geometry;  $I_{\text{tot},i}$  is the total intensity of the  $L_i$  line;  $\beta$  is the anisotropy parameter of the considered x-ray line;  $\alpha$  is the anisotropy coefficient of the  $i$ th line, which depends on the total angular momentum  $j$  of the initial and final vacancy states of the target atom;  $\kappa$  is the Coster-Kronig (CK) correction coefficient; and  $P_2(\cos\theta)$  is the second-order Legendre polynomial, expressed by

$$P_2(\cos\theta) = \frac{1}{4}[3\cos(2\theta) + 1]. \quad (3)$$

Up to now, most experimental studies have focused on the alignment properties of atoms in photoionization, electron-impact ionization, and light-ion impacts with an incident energy greater than 300 keV. For a light-ion impact on medium- and high- $Z$  atoms, the alignment has often been investigated with a nuclear charge number greater than 47 by many groups [6,7,13–16]. In theory, predictions based on the plane-wave Born approximation (PWBA) [17] and semiclassical treatment are often employed for calculation [18]. For

\*wangxingcn@xjtu.edu.cn

TABLE I. Energies (keV) of the  $L$ -subshell edges and the  $L_{\alpha 1}$ ,  $L_{\alpha 2}$ ,  $L_{\beta 1}$ ,  $L_{\beta 2}$ , and  $L_{\gamma 1}$  characteristic x rays for  $^{42}\text{Mo}$ ,  $^{48}\text{Cd}$ , and  $^{49}\text{In}$  [27].

| Designation            | Energy (keV)     |                  |                  |
|------------------------|------------------|------------------|------------------|
|                        | $^{42}\text{Mo}$ | $^{48}\text{Cd}$ | $^{49}\text{In}$ |
| $L_1$ edge             | 2.8806(50)       | 4.01901(19)      | 4.23726(21)      |
| $L_2$ edge             | 2.62730(82)      | 3.72801(17)      | 3.93932(19)      |
| $L_3$ edge             | 2.52356(76)      | 3.53760(15)      | 3.73025(17)      |
| $L_3M_5(L_{\alpha 1})$ | 2.293187(50)     | 3.133755(47)     | 3.286982(52)     |
| $L_3M_4(L_{\alpha 2})$ | 2.289875(50)     | 3.126950(70)     | 3.279322(77)     |
| $L_2M_4(L_{\beta 1})$  | 2.394831(55)     | 3.316605(53)     | 3.487244(58)     |
| $L_3N_5(L_{\beta 2})$  | 2.51833(15)      | 3528.159(59)     | 3.713847(49)     |
| $L_2N_4(L_{\gamma 1})$ | 2.62352(16)      | 3.716898(99)     | 3.920848(73)     |

example, Jitschin *et al.* studied the alignment of Xe, Dy, and Au within the proton energy range from 250 keV to 6 MeV, and they found that the results are in fair agreement with PWBA calculations [6]. As a matter of fact, the total ionization cross section is insensitive to the projection of angular momentum of the ionized atom since it is an average over the magnetic states. The current measurements of x-ray production or inner-shell ionization cross sections [19–26] ought to take the angular dependence of characteristic radiation into consideration to eliminate systematic errors, although it has been suggested that the errors are evaluated to be small except in special cases [8].

In the present work, the alignment parameter  $\mathcal{A}_{20}$  for  $^{42}\text{Mo}$ ,  $^{48}\text{Cd}$ , and  $^{49}\text{In}$  ions with a vacancy in the  $L_3$  subshell has been measured by proton impact in the low-energy region from 100 to 250 keV. It is derived from the angular distributions of the transition of  $L_3$  vacancies to the  $M_4$ ,  $M_5$ , and  $N_5$  subshells, denoted, respectively, as  $L_{\alpha 2}$ ,  $L_{\alpha 1}$ , and  $L_{\beta 2}$ , whose energies are shown in Table I. This work reveals the existence of atomic alignment by proton impact at an incident energy even lower than 300 keV. Finally, experimental results are compared with the semiclassical theory of inner-shell ionization.

## II. EXPERIMENT

The experiment was conducted with the 320-kV Electron Cyclotron Resonance (ECR) ion-source platform at the Institute of Modern Physics (IMP) in Lanzhou. Protons with energies of 100, 150, 200, 225, and 250 keV are selected for the measurements. The ions are extracted from the ECR ion source; then they are mass analyzed with two  $90^\circ$  sector magnets, focused by two quadrupole lenses and deflected by another  $60^\circ$  sector magnet into the experimental chamber. The beam can be collimated to a divergence of about  $0.7^\circ$  using a pair of four-jaw slits. The schematic diagram of the experimental setup is presented in Fig. 1. Here  $\theta$  is the emission angle between the incident beam and emitted x rays.

Targets of  $^{42}\text{Mo}$ ,  $^{48}\text{Cd}$ , and  $^{49}\text{In}$  mounted on a three-dimensional movable target holder are set perpendicular to the beam axis in the center of an ultrahigh-vacuum chamber with a pressure of  $10^{-8}$  mbar. The emitted x rays are measured by

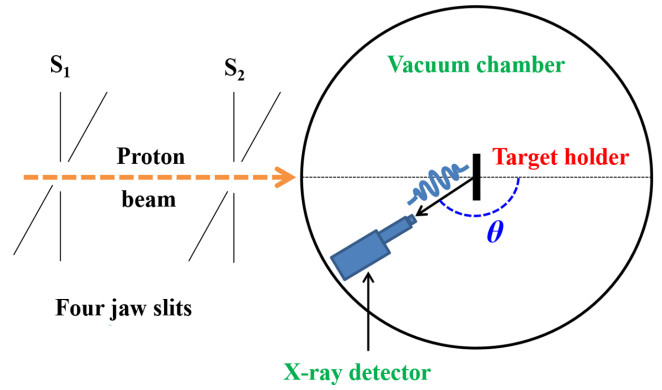


FIG. 1. Schematic diagram of the experimental setup.

an AMPTEK production silicon drift detector (XR-100SDD) with an energy resolution of about 136 eV@5.9 keV and a solid angle of 0.0066 sr. The detection efficiency for x-ray energy from 1 to 10 keV is presented in Fig. 2, and it is more than 80% in this measurement [28].

Since the energy difference of the  $L_{\alpha 1}(L_3M_5)$  and  $L_{\alpha 2}(L_3M_4)$  lines originating from the  $L_3$  subshell is less than 8 eV in this work, they cannot be resolved by the detector and are treated as a single peak  $L_{\alpha}$ . The typical  $L_{\alpha}(L_3M_{4,5})$ ,  $L_{\beta 1}(L_2M_4)$ ,  $L_{\beta 2}(L_3N_5)$ , and  $L_{\gamma 1}(L_2N_4)$  x-ray lines are detected geometrically at emission angles from  $115^\circ$  to  $155^\circ$ .

## III. RESULTS AND DISCUSSION

### A. Determination of the alignment parameter from measured x-ray spectra

Typical spectra for three targets are measured at different emission angles to study x-ray angular distributions. In order to investigate the influence of energy on the alignment parameter, the measurements were made at different incident energies. Here the measured characteristic  $L$  x-ray spectrum

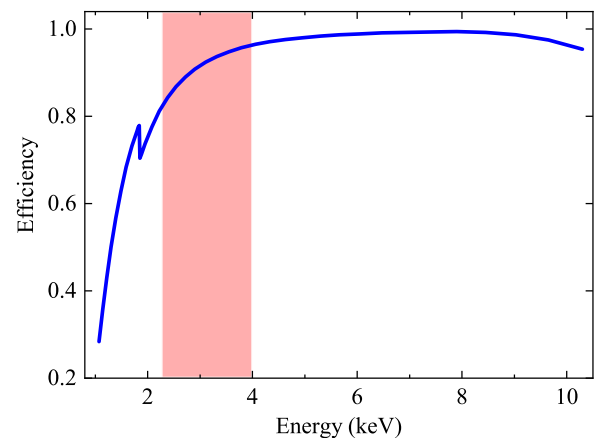


FIG. 2. Efficiency of the 450- $\mu\text{m}$ -thick silicon drift detector. The x-ray detector has an active crystal area of  $25\text{ mm}^2$ . A beryllium window with a thickness of  $12.5\text{ }\mu\text{m}$  is integrated in the x-ray detector to improve the signal-to-noise ratio. The detection efficiency of the measurement in this work is indicated in red shaded area.

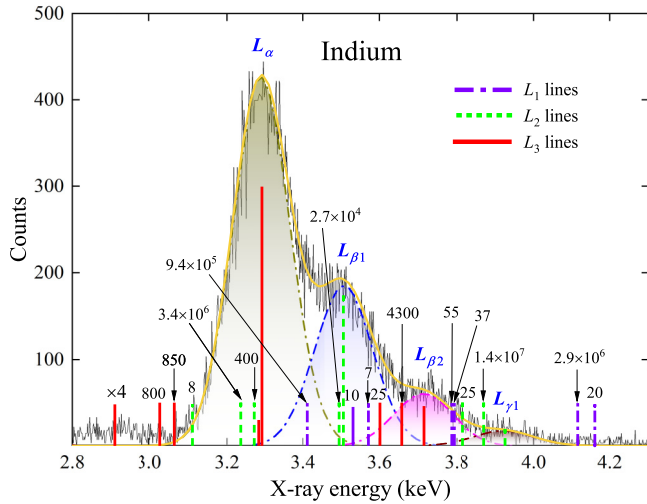


FIG. 3. Characteristic  $L$  x-ray spectrum of an indium target at an incident energy of 200 keV.  $L_{\alpha}$ ,  $L_{\beta_1}$ ,  $L_{\beta_2}$ , and  $L_{\gamma_1}$  x rays are distinguished and marked above the peak. The vertical lines on the bottom indicate the intensities of different transitions involving vacancy filling to the  $L$  subshell. Except for four dominant lines, the value above each line depicts the magnification of the relative intensity. The dash-dotted violet, dotted green, and solid red lines represent the  $L_1$ ,  $L_2$ , and  $L_3$  lines, respectively. CK probabilities and x-ray emission rates are taken from Refs. [31,32] for the derivation of the x-ray intensities.

of In at different emission angles is synthesized for an incident energy of 200 keV and is shown in Fig. 3. It can be seen that four prominent peaks, namely,  $L_{\alpha}$  ( $L_3M_{4,5}$ ),  $L_{\beta_1}$  ( $L_2M_4$ ),  $L_{\beta_2}$  ( $L_3N_5$ ), and  $L_{\gamma_1}$  ( $L_2N_4$ ), are clearly distinguished, while other lines are too weak to be observed. According to the peak energies in Table I and the resolution of the x-ray detector employed in this work, the x-ray peak areas can be quantitatively determined with a multi-Gaussian least-squares fitting procedure. The FWHM of the  $L_{\alpha}$ ,  $L_{\beta_1}$ ,  $L_{\beta_2}$ , and  $L_{\gamma_1}$  lines are, respectively, 149.8, 151.7, 153.4, and 155.0 eV, which is consistent with the energy resolution of the x-ray detector. Measurements of  $L$  x rays with high resolution have been performed for indium using a grating x-ray spectrometer [29] and cadmium using a wavelength-dispersive spectrometer [30]. In order to evaluate the contaminations due to the isotropic or nonisotropic transitions in the four measured peaks, the contributions of different transitions are calculated with  $L$ -subshell ionization cross sections, CK probabilities, and x-ray emission rates [31,32]. One can easily infer from Fig. 3 that the contribution of contaminating lines to the four measured peaks is much less than 1%.

$L_{\beta_1}$  and  $L_{\gamma_1}$  lines originating from the  $2p_{1/2}$  ( $j = 1/2$ ) subshell are expected to show isotropic emissions. The experimental results actually demonstrate that both lines are found to have isotropic emissions spatially within the uncertainties in the measurement. Thus, the  $L_{\beta_1}$  x-ray intensity at each emission angle is taken to be a good reference to eliminate the geometry misalignment, if any, in the experimental setup. Therefore, the angular distributions of intensity ratios  $dI(L_{\alpha})/dI(L_{\beta_1})$  and  $dI(L_{\beta_2})/dI(L_{\beta_1})$  are investigated in the present work. The experimental values of the differential x-ray

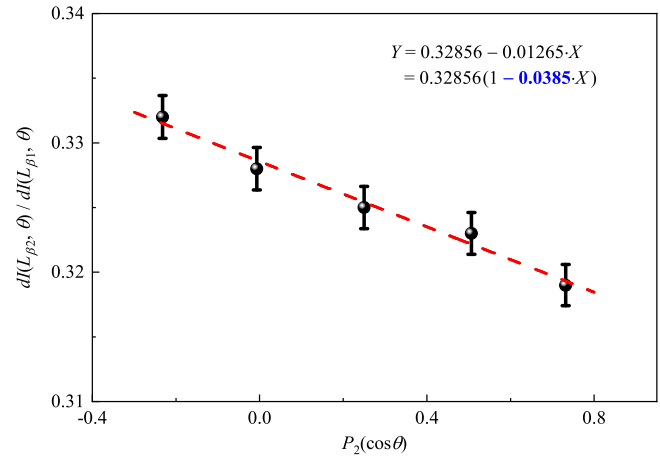


FIG. 4. Differential intensity ratio of  $dI(L_{\beta_2}, \theta)/dI(L_{\beta_1}, \theta)$  as a function of  $P_2(\cos\theta)$  for 200-keV proton impact on In. The emission angle is from  $115^\circ$  to  $155^\circ$  at an interval of  $10^\circ$ . The symbols with error bars are the measured values. The dashed red curve is the fitting of experimental results with the linear function, and the function expression is presented inside the figure.

intensity ratio  $dI(L_i)/dI(L_{\beta_1})$  can be expressed by

$$\frac{dI(L_i)}{dI(L_{\beta_1})} = \frac{\frac{N(L_i)}{\varepsilon(L_i)N(p)}}{\frac{N(L_{\beta_1})}{\varepsilon(L_{\beta_1})N(p)}} = \frac{N(L_i)\varepsilon(L_{\beta_1})}{N(L_{\beta_1})\varepsilon(L_i)}. \quad (4)$$

Here  $N(L_i)$  and  $N(L_{\beta_1})$  are the net counts of the  $L_i$  and  $L_{\beta_1}$  x-ray lines in the measured x-ray spectra;  $\varepsilon(L_i)$  and  $\varepsilon(L_{\beta_1})$  are the detection efficiencies for the  $L_i$  and  $L_{\beta_1}$  x rays, and  $N_p$  is the number of counts of incident protons. Since the x-ray energies are very close to one another and thin targets are employed in this work, the self-absorption effect of x rays inside the target can be approximately counteracted in the intensity ratios. The total experimental error for x-ray intensities is assessed to be about 4%, combining statistical error (1%, considering the numbers of incident protons and emitted x rays) with errors estimated for the solid angle (2%), background subtraction (2%), and fitting procedure (1%).

From Eqs. (2) and (4), the differential intensity ratio  $dI(L_i, \theta)/dI(L_{\beta_1}, \theta)$  for the  $L_i$  x-ray line at emission angle  $\theta$  can consequently be written as

$$\begin{aligned} \frac{dI(L_i, \theta)}{dI(L_{\beta_1}, \theta)} &= \frac{N(L_i)\varepsilon(L_{\beta_1})}{N(L_{\beta_1})\varepsilon(L_i)} = a_i + b_i P_2(\cos\theta) \\ &= a_i[1 + \beta P_2(\cos\theta)], \end{aligned} \quad (5)$$

where  $a_i = \frac{I_{\text{tot},i}}{I_{\alpha,\beta_1}}$  and  $\beta = \frac{b_i}{a_i}$ . Therefore, the anisotropy parameter  $\beta$  can be determined experimentally by investigating the dependence of differential intensity ratios on  $P_2(\cos\theta)$ . Figure 4 depicts the differential intensity ratio of  $dI(L_{\beta_2}, \theta)/dI(L_{\beta_1}, \theta)$  as a function of  $P_2(\cos\theta)$  for 200-keV proton impact on an In target. According to Eq. (5), the function is supposed to be linear mathematically. Then, the experimental values are fitted with a linear function, and  $R^2$  is 0.978. This demonstrates a good linear relationship between the differential intensity ratio and  $P_2(\cos\theta)$ . Consequently, the anisotropy parameter  $\beta$  is determined to be  $-0.0385$  for the  $L_{\beta_2}$  line according to Eq. (5), as shown in Fig. 4. For  ${}_{42}\text{Mo}$ ,

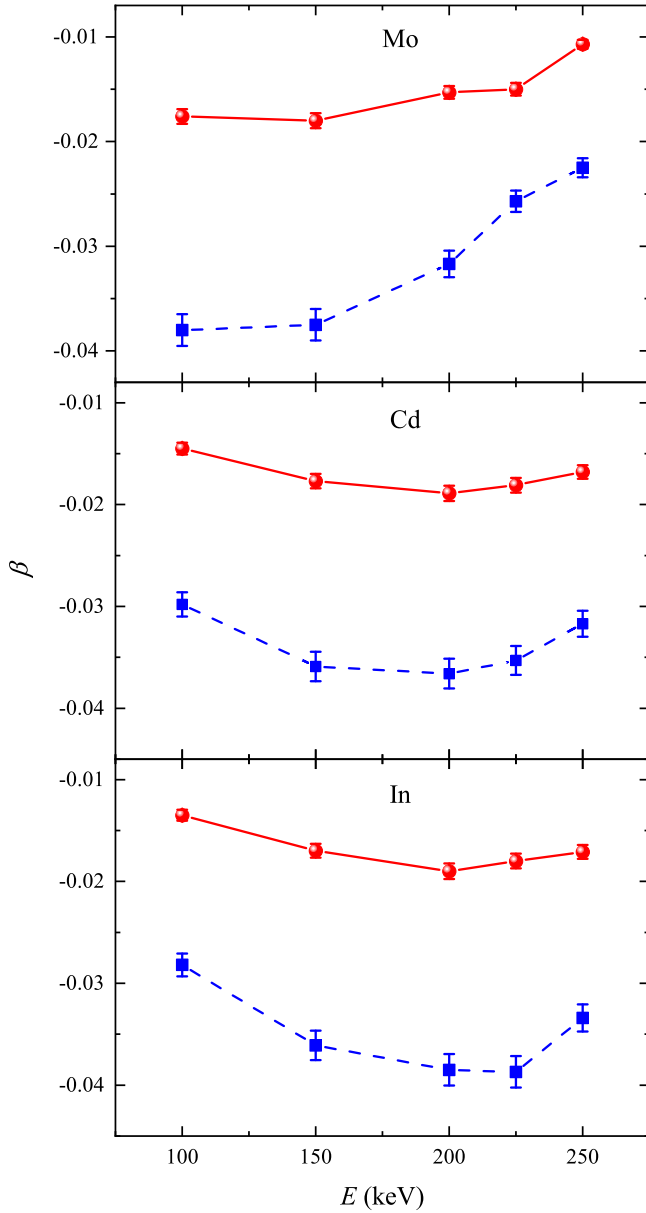


FIG. 5. Anisotropy parameters  $\beta$  as a function of incident energy for  ${}_{42}\text{Mo}$ ,  ${}_{48}\text{Cd}$ , and  ${}_{49}\text{In}$  targets. The red spheres and blue squares represent anisotropy parameters for the  $L_\alpha$  and  $L_{\beta 2}$  lines, respectively. The solid red line and dashed blue line illustrate only the trend.

${}_{48}\text{Cd}$ , and  ${}_{49}\text{In}$  targets, the anisotropy parameters of the  $L_\alpha$  and  $L_{\beta 2}$  lines are plotted as a function of incident energy in Fig. 5. The experimental value versus incident energy almost has the same variation tendency for both lines of each target. For  ${}_{48}\text{Cd}$  and  ${}_{49}\text{In}$  with adjacent atomic numbers, it decreases first and then increases in the projectile-energy regime of 100–250 keV, while for  ${}_{42}\text{Mo}$ , the value increases monotonically for the  $L_{\beta 2}$  line. In addition, it can be inferred that the anisotropy parameters of the  $L_{\beta 2}$  line are almost two times higher than the value of the  $L_\alpha$  line for all three collision systems.

In the following the anisotropy parameter  $\beta$  ( $=\alpha\kappa\mathcal{A}_{20}$ ) should be converted to the alignment parameter  $\mathcal{A}_{20}$ . In proton-impact ionization, the vacancy in the  $L_3$  subshell can originate not only from direct ionization but also from vacancy

TABLE II. Calculated ionization cross sections (barns) for  $L$  subshells in different collision systems using the program ERCS08 [33].

| System               | Energy (keV) | $\sigma_{L_1}$ | $\sigma_{L_2}$ | $\sigma_{L_3}$ |
|----------------------|--------------|----------------|----------------|----------------|
| $p+{}_{42}\text{Mo}$ | 100          | 4.692          | 4.735          | 13.54          |
|                      | 150          | 14.02          | 28.19          | 75.95          |
|                      | 200          | 21.27          | 77.83          | 202.3          |
|                      | 225          | 24.24          | 112.5          | 288.5          |
|                      | 250          | 27.77          | 153.2          | 388.7          |
| $p+{}_{48}\text{Cd}$ | 100          | 0.598          | 0.335          | 1.138          |
|                      | 150          | 3.227          | 3.143          | 9.777          |
|                      | 200          | 6.864          | 11.05          | 32.62          |
|                      | 225          | 8.535          | 17.39          | 50.32          |
|                      | 250          | 9.978          | 25.40          | 72.30          |
| $p+{}_{49}\text{In}$ | 100          | 0.413          | 0.212          | 0.744          |
|                      | 150          | 2.462          | 2.161          | 6.912          |
|                      | 200          | 5.562          | 7.935          | 24.01          |
|                      | 225          | 7.072          | 12.68          | 37.56          |
|                      | 250          | 8.413          | 18.75          | 54.58          |

transfer from the  $K$  to  $L$  shell or from the CK transition from  $L_1$  and  $L_2$  subshells. Since the  $K$ -shell ionization cross section in this work is almost 6 orders of magnitude lower than the  $L$  subshell ionization cross sections estimated with the program ERCS08 [33], only the CK transition is considered for the evaluation of the correction coefficient. As a result, the factor  $\kappa$  is expressed by

$$\kappa = \frac{\sigma_{L_3}}{\sigma_{L_3}^{\text{total}}} = \frac{\sigma_{L_3}}{\sigma_{L_1}(f_{12}f_{23} + f_{13}) + \sigma_{L_2}f_{23} + \sigma_{L_3}}, \quad (6)$$

where  $\sigma_{L_3}$  is the ionization cross section from direct ionization in the  $L_i$  subshell by proton impact and  $\sigma_{L_3}^{\text{total}}$  is the total probability for vacancy production in the  $L_3$  subshell. This factor is evaluated using ionization cross sections calculated by ECPSSR theory [33], which considers the projectile energy loss ( $E$ ) and Coulomb deflection ( $C$ ) as well as the perturbed stationary state (PSS) and relativistic (R) nature of the target electron for direct ionization of atomic electrons by projectile ions. The ionization cross sections for the  $L_i$  subshells are shown in Table II for three collision systems in the energy regime of 100–250 keV. In addition, CK transition probabilities  $f_{ij}$  are given in Table III [34,35].

Besides the factor  $\kappa$ , the coefficient  $\alpha$  in Eq. (2) also connects the measured anisotropy of the x-ray line to the alignment parameter of the vacancy. For target atoms with high atomic numbers, the fine-structure interaction is adequately strong to couple spin and orbital angular momenta to  $j$

TABLE III. Theoretical Coster-Kronig yields  $f_{ij}$  for  $L$  subshells for  ${}_{42}\text{Mo}$ ,  ${}_{48}\text{Cd}$ , and  ${}_{49}\text{In}$  targets taken from Refs. [34,35].

| Element            | $f_{12}$ | $f_{13}$ | $f_{23}$ |
|--------------------|----------|----------|----------|
| ${}_{42}\text{Mo}$ | 0.048    | 0.692    | 0.126    |
| ${}_{48}\text{Cd}$ | 0.051    | 0.785    | 0.158    |
| ${}_{49}\text{In}$ | 0.052    | 0.784    | 0.160    |

TABLE IV. The coefficient  $\alpha$  as employed in Eq. (2) for single and combined x-ray lines.

| Line          | ${}_{42}\text{Mo}$ | ${}_{48}\text{Cd}$ | ${}_{49}\text{In}$ |
|---------------|--------------------|--------------------|--------------------|
| $L_{\alpha}$  | 0.050(2)           | 0.050(4)           | 0.050(4)           |
| $L_{\beta 2}$ | 0.1                | 0.1                | 0.1                |

eigenstates. The value  $\alpha$  for transitions between  $j$  eigenstates are 0.1,  $-0.4$ , and 0.1 for  $L_{\alpha 1}$ ,  $L_{\alpha 2}$ , and  $L_{\beta 2}$ , respectively [4]. For unresolved  $L_{\alpha}$  lines the coefficient  $\alpha$  is determined as the sum of the  $\alpha$  values for the  $L_{\alpha 1}$  and  $L_{\alpha 2}$  lines, weighted by the corresponding emission rates [31,32]. The  $\alpha$  values for  ${}_{42}\text{Mo}$ ,  ${}_{48}\text{Cd}$ , and  ${}_{49}\text{In}$  are almost equal, and a summary of the values used in this measurement is given in Table IV.

For the sake of comparison between different collision systems, the incident energy is characterized by the scaled projectile velocity  $V = v_p/v_{L_3}$ , where  $v_p$  is the projectile velocity and  $v_{L_3} = (\frac{2E_{L_3}}{m_e})^{\frac{1}{2}}$  is the classical orbiting velocity of the  $L_3$  electron as calculated from the binding energy  $E_{L_3}$  and electron mass  $m_e$ . Consequently, the measured alignment parameter corresponding to different scaled projectile velocities is shown in Table V for three collision systems.

### B. Framework of the semiclassical theory of inner-shell ionization

The measurements of the alignment parameter are compared with the semiclassical theory of inner-shell ionization. Coulomb-deflection effects are appropriately considered using hyperbolic classical orbitals, while the electron in the initial and final states is treated with screened relativistic hydrogenic wave functions.

The total ionization cross section  $\sigma_{L_i}^i(\mu_{i'})$  for the  $L - i$  subshell with magnetic quantum number  $\mu_{i'}$  is given in a quantum-mechanical treatment as [13,18]:

$$\sigma_{L_i}^i(\mu_{i'}) = \int \frac{1}{2\pi} \frac{m_p^{*2}}{(2\pi\hbar)^4} \frac{E_e}{(\hbar c)^2} q \frac{Q_f}{Q_{i'}} \times \sum_{\tau_f} |T_{Q_f, q; Q_{i'}}(\mu_{i'}, \tau_f)|^2 d\Omega_e dE_e d\Omega_p, \quad (7)$$

where  $q$  is the wave number of the free electron with energy  $E_e$  and polarization  $\tau_f$ .  $Q_{i'}$  and  $Q_f$  are the relative momenta in the initial and final states, respectively. The  $T$  matrix leading

TABLE V. Alignment parameter  $\mathcal{A}_{20}$  derived using Eq. (2) for proton impact on  ${}_{42}\text{Mo}$ ,  ${}_{48}\text{Cd}$ , and  ${}_{49}\text{In}$ . The listed errors of  $\mathcal{A}_{20}$  do not contain the uncertainty of parameter  $\alpha$ , which is 4% for the  $L_{\alpha}$  line for Mo and 8% for Cd and In. The CK correction coefficient  $\kappa$  is also given.

| System               | Energy (keV) | $V^2$  | $\kappa$ | $\mathcal{A}_{20}$ |
|----------------------|--------------|--------|----------|--------------------|
| $p+{}_{42}\text{Mo}$ | 100          | 0.0216 | 0.778    | $-0.471(16)$       |
|                      | 150          | 0.0324 | 0.851    | $-0.432(12)$       |
|                      | 200          | 0.0432 | 0.891    | $-0.350(14)$       |
|                      | 225          | 0.0486 | 0.903    | $-0.289(12)$       |
|                      | 250          | 0.0540 | 0.909    | $-0.241(12)$       |
| $p+{}_{48}\text{Cd}$ | 100          | 0.0154 | 0.683    | $-0.431(15)$       |
|                      | 150          | 0.0231 | 0.762    | $-0.469(13)$       |
|                      | 200          | 0.0308 | 0.822    | $-0.452(13)$       |
|                      | 225          | 0.0346 | 0.841    | $-0.425(11)$       |
|                      | 250          | 0.0385 | 0.858    | $-0.381(12)$       |
| $p+{}_{49}\text{In}$ | 100          | 0.0146 | 0.673    | $-0.410(17)$       |
|                      | 150          | 0.0219 | 0.751    | $-0.467(13)$       |
|                      | 200          | 0.0292 | 0.809    | $-0.473(14)$       |
|                      | 225          | 0.0329 | 0.831    | $-0.449(12)$       |
|                      | 250          | 0.0365 | 0.850    | $-0.398(12)$       |

from the initial state, determined by the bound electron and projectile wave function,  $\varphi_{i'}(\mu_{i'})$  and  $\chi_{Q_{i'}}^{(+)}$ , respectively, to the final state described by the free-electron wave function  $\varphi_q^{(-)}(\tau_f)$  and the projectile wave function  $\chi_{Q_f}^{(-)}$  is expressed as

$$T_{Q_f, q; Q_{i'}}(\mu_{i'}, \tau_f) = \langle \varphi_q^{(-)}(\tau_f) \chi_{Q_f}^{(-)} | U(r, R) | \varphi_{i'}(\mu_{i'}) \chi_{Q_{i'}}^{(+)} \rangle. \quad (8)$$

The residual interaction  $U(r, R)$  including recoil effects is written as [14,18]

$$U(r, R) = \frac{Z_p Z_t e^2}{\left| R + \frac{m_e}{m_e + m_t} r \right|} - \frac{Z_p e^2}{\left| R - \frac{m_t}{m_e + m_t} r \right|}. \quad (9)$$

Here  $Z_t$  and  $Z_p$  are the charges of the target with mass  $m_t$  and the projectile with mass  $m_p$ , respectively.  $m_e$  is the electron mass, and  $m_p^*$  is the reduced mass of the projectile and target system. The vector between the target and projectile is denoted by  $R$ , while  $r$  is the vector between the target and electron.

The cross section is now calculated in a semiclassical approximation (SCA). The result can be derived with Dirac wave functions for the electron states:

$$\begin{aligned} \sigma_{L_k}^i(\mu_{i'}) &= 64\pi \left( \frac{m_p^*}{m_e} \right)^2 (Z_p \alpha')^2 (2j_{i'} + 1)^2 \int_1^\infty \varepsilon d\varepsilon \int_0^{T_e^{\max}} dT_e \left( 1 + \frac{1}{2} T_e \right) a_c^2 \frac{\bar{q}}{Q_i'} \frac{Q_f}{Q_{i'}} \sum_{\lambda_{i'f}} (2j_f + 1) \\ &\times \left| \sum_l \frac{1}{\sqrt{2l+1}} \frac{1}{2} (1 + (-)^{l'+l_f+l}) \begin{pmatrix} j_f & l & j_{i'} \\ -\lambda - \mu_{i'} & \lambda & \mu_{i'} \end{pmatrix} \begin{pmatrix} j_f & l & j_{i'} \\ \frac{1}{2} & 0 & -\frac{1}{2} \end{pmatrix} \right. \\ &\times \left. \sum_{\lambda'} Y_{l\lambda'} \left( \frac{\pi}{2}, \frac{\pi + \theta_p}{2} \right) d_{\lambda\lambda'}^l \left( \frac{\pi}{2} \right) I_{i'f}^{l\lambda'}(\varepsilon, \xi, \bar{a}_c) \right|^2. \end{aligned} \quad (10)$$

In this equation, semiclassical quantities have been introduced as follows:

$$Q = \frac{Q_{i'} + Q_f}{2}, \quad \eta = \frac{\eta_{i'} + \eta_f}{2}, \quad \eta_{i',f} = \frac{Z_p Z_t e^2 m_p^*}{\hbar^2 Q_{i',f}},$$

$$a_c = \frac{\eta}{Q}, \quad \xi = \eta_f - \eta_{i'} = a_c(Q_{i'} - Q_f), \quad \varepsilon = \frac{1}{\sin \frac{\theta_p}{2}},$$

$$b = -a\sqrt{\varepsilon^2 - 1}. \quad (11)$$

Here the quantum numbers of the electron in the initial and final states are given by  $i_{i'}$ ,  $j_{i'}$ , and  $l_{i'}$  and  $i_f$ ,  $j_f$ , and  $l_f$ , respectively.  $\alpha'$  is the fine-structure constant. For the quantities defining the hyperbolic trajectory,  $\varepsilon$  is the eccentricity.  $\theta_p$ ,  $a$ , and  $b$  denote the scattering angle, semimajor axis ( $<0$ ), and impact parameter, respectively. The kinetic energy of the final electron is denoted by  $T_e$ , and  $I_{i'i_f}^{\lambda'}$ ( $\varepsilon, \xi, \bar{a}_c$ ) is the classical integral over the radial electron form factor along the symmetrized hyperbolic trajectory of the projectile [13,18].

In this semiclassical model, the Coulomb-deflection effect can be exactly considered by utilizing the correct hyperbolic classical trajectory in the low-impact-energy regime [14]. Therefore, it is well suited for the theoretical prediction of the alignment in this work. In fact, the theory incorporating appropriate treatment of the projectile trajectory can reproduce experimental alignment data for light-ion impact at all collision velocities. In addition, the theory allows us to explore the impact parameter dependence of the excitation or ionization probability. The effect of the recoil of the target has been taken into account in the SCA theory, where it turns out that the effect is small enough that it can be neglected for the total alignment. The recoil effect appears clearly only at very small impact parameters ( $b < 50$  fm) for the impact-parameter-dependent alignment. Although there is some difference when one uses screened hydrogenic or relativistic Hartree-Fock-Slater wave functions in the resulting ionization probabilities, the difference becomes much smaller for the derived alignment parameters. In general, the distinction between the different choices of the wave function is much smaller than the experimental errors [14], but for the alignment of the  $M_{3,4,5}$  subshell these effects are stronger due to the more complex nature of the electron wave functions [36].

As a consequence, Eq. (10) is employed in this work for the calculation of the alignment in addition to Eq. (1).

### C. Analysis and discussion of experimental and theoretical results

The experimental data are compared with theoretical prediction based on the numerical evaluation of Eqs. (1) and (10). The semiclassical theory accounts for binding corrections and screening effects which are simulated by an effective charge of the target used for the Dirac wave functions of the electron. Figure 6 displays measured alignment parameters for  $^{42}\text{Mo}$ ,  $^{48}\text{Cd}$ , and  $^{49}\text{In}$  targets as a function of the square of the scaled projectile velocity  $V$ . It is found that good agreement with the theory is obtained even for small impact energies where the Coulomb-deflection effect becomes important. Theoretical predictions for the three targets are similar in value and

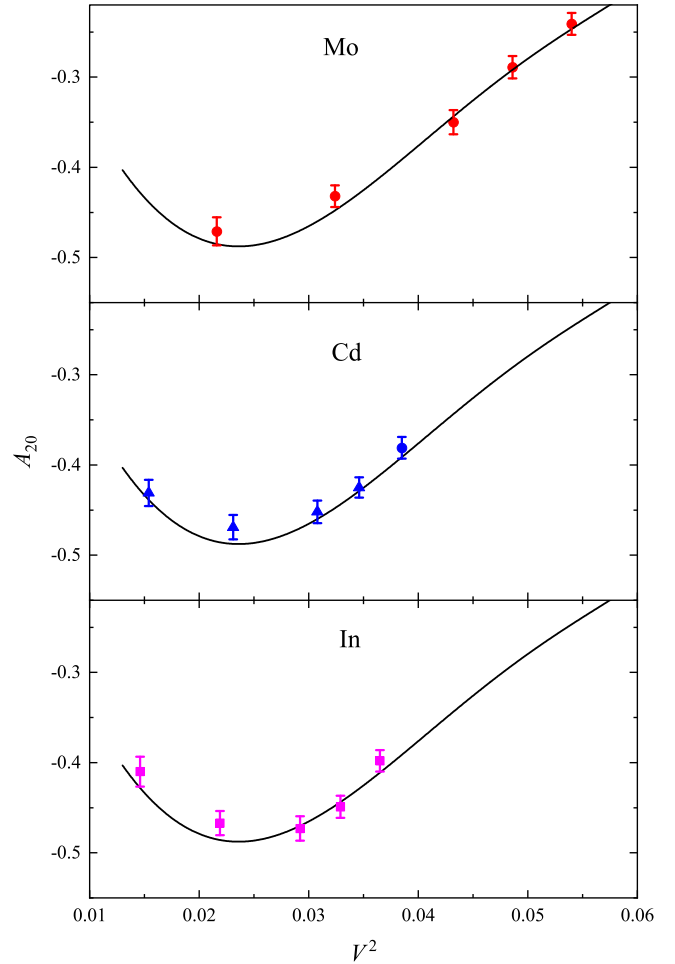


FIG. 6. Alignment parameter  $\mathcal{A}_{20}$  of  $^{42}\text{Mo}$ ,  $^{48}\text{Cd}$ , and  $^{49}\text{In}$  as a function of the square of the scaled projectile velocity  $V$ . The solid curves are the predictions of the semiclassical theory. The symbols with error bars are the experimental values in the present work. The displayed errors for  $\mathcal{A}_{20}$  do not contain the uncertainty of parameter  $\alpha$ , which is 4% for the  $L_\alpha$  line for Mo and 8% for Cd and In.

tendency, especially for  $^{48}\text{Cd}$  and  $^{49}\text{In}$ , which have adjacent atomic numbers.

The experimental results present the evolution of  $\mathcal{A}_{20}$  with proton energy in the low-energy region. The energy range of the impact velocities studied covers the inflection point of the alignment. One can explicitly observe that the values decrease first and then increase for  $^{48}\text{Cd}$  and  $^{49}\text{In}$  in both experiment and theory. It should be mentioned that the sign of  $\mathcal{A}_{20}$  is negative in this work. The degree of the alignment is maximal at  $V^2 \approx 0.023$  in the present experimental conditions.

The alignment parameter reflects the relative difference of the ionization cross sections  $\sigma(j, m_j)$ . It can be inferred that the difference reaches the maximum at a velocity of  $0.15v_{L_3}$  for proton impact in this measurement, and  $\sigma(\frac{3}{2}, \frac{3}{2})$  is less than  $\sigma(\frac{3}{2}, \frac{1}{2})$  because of the negative alignment. When the velocity approaches zero, the alignment will also tend to zero since ionization cross sections at magnetic substates  $m_j = 3/2$  and  $m_j = 1/2$  are close to zero simultaneously.

In addition, a small discrepancy around the inflection point of the alignment parameter is found between the experiment

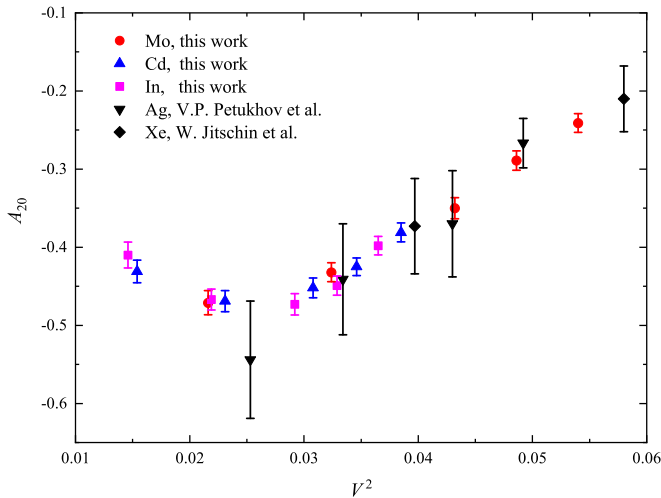


FIG. 7. Proton-impact-induced alignment of medium- $Z_t$  elements as a function of the square of the scaled projectile velocity  $V$ . The results obtained by Jitschin *et al.* [6] and Petukhov *et al.* [15] are also shown for comparison.

and theory in Fig. 6. It is attributed to the use of atomic parameters for single ionization in the CK correction coefficient. Compared with photoionization and electron-impact ionization, the CK rates are expected to be lower, and the fluorescence yields are expected to increase for multiply ionized atoms since the existence of outer vacancies reduces the possible Auger processes more effectively than radiative transitions [37]. Thus, the CK yields in Eq. (6) becomes smaller, and the factor  $\kappa$  actually moves closer to unity. The variation of the CK rates and fluorescence yields will influence the determination of the alignment value to a certain extent in the experimental theoretical evaluation according to Eqs. (2) and (10). As a result, multiple ionization, i.e., additional vacancies in  $L$  or higher shells, creates a more complex situation which should be considered in theoretical CK yields and models for inner-shell ionization.

The alignment values measured for all three target elements are plotted in Fig. 7. It shows a good scaling property of the alignment. The results for  $\mathcal{A}_{20}$  are also compared with

other measurements of medium- $Z_t$  elements by Jitschin *et al.* [6] and Petukhov *et al.* [15] since the nuclear charge numbers of Ag and Xe are close to the numbers of this work. Good agreement is found for both the tendency and values. Semi-classical treatment of the proton-induced alignment of the  $L_3$  subshell is an accurate description even for ultralow incident energy as a whole.

#### IV. CONCLUSION

The investigation of the alignment parameter  $\mathcal{A}_{20}$  after  $L_3$  subshell ionization was conducted experimentally using the proton impact on  $^{42}\text{Mo}$ ,  $^{48}\text{Cd}$ , and  $^{49}\text{In}$  in the velocity range of  $(2.00\text{--}3.16)v_B$  ( $v_B$  is the Bohr velocity). It was found that the angular distribution of the differential intensity ratios  $L_{\alpha}/L_{\beta 1}$  and  $L_{\beta 2}/L_{\beta 1}$  is proportional to the second-order Legendre polynomial  $P_2(\cos\theta)$ . Then, the anisotropy parameters are derived for incident energy from 100 to 250 keV. The experimental alignment parameters were obtained by applying the CK correction factor and anisotropy coefficients for the considered transitions. The sign of  $\mathcal{A}_{20}$  is negative in the range of impact velocities studied. Compared with the semiclassical theory of inner-shell ionization, satisfactory agreement was found within the whole region of incident energies. The results demonstrate that the highest alignment parameter appears at  $V^2 \approx 0.023$  under the present experimental conditions. A small discrepancy around the inflection point of the alignment parameter was observed and attributed to the atomic parameters employed only for single ionization in the CK correction coefficient. Atomic parameters for multiple ionization would be more appropriate for the deduction of the alignment parameter in experiment.

#### ACKNOWLEDGMENTS

The authors are grateful for the technical support from the group of the 320-kV high-voltage platform at IMP-CAS in Lanzhou. This work is supported by the Natural Science Basic Research Plan in Shaanxi Province of China (Program No. 2018JM1027) and the National Natural Science Foundation of China (Grants No. 11875219 and No. 11405123).

- 
- [1] M. Lv, B. Xu, L. Cai, X. Guo, and X. Yuan, *Appl. Surf. Sci.* **439**, 780 (2018).
  - [2] H. Shin, I. Song, Y. An, and W. Choe, *Fusion Eng. Des.* **153**, 111459 (2020).
  - [3] B. Yang, D. Yu, C. Shao, Y. S. Kozhedub, Y. Xue, W. Wang, M. Zhang, J. Liu, Z. Song, R. Lu, F. Ruan, Y. Wu, and X. Cai, *Phys. Rev. A* **102**, 042803 (2020).
  - [4] E. G. Berezhko and N. M. Kabachnik, *J. Phys. B* **10**, 2467 (1977).
  - [5] E. G. Berezhko, N. M. Kabachnik, and V. V. Sizov, *J. Phys. B* **11**, L421 (1978).
  - [6] W. Jitschin, H. Kleinpoppen, R. Hippler, and H. O. Lutz, *J. Phys. B* **12**, 4077 (1979).
  - [7] W. Jitschin, A. Kaschuba, H. Kleinpoppen, and H. O. Lutz, *Z. Phys. A* **304**, 69 (1982).
  - [8] S. F. Barros, V. R. Vanin, A. Mangiarotti, N. L. Maidana, and J. M. Fernández-Varea, *Phys. Rev. A* **100**, 062705 (2019).
  - [9] G. Sestric, S. Ferguson, I. Wright, and S. Williams, *Radiat. Phys. Chem.* **102**, 40 (2014).
  - [10] Y. Liu, Z. Xu, X. Wang, and L. Zeng, *Nucl. Instrum. Methods in Phys. Res., Sect. B* **446**, 1 (2019).
  - [11] X. Wang, Z. Xu, Y. Zhang, C. Ma, and C. Zhu, *Radiat. Phys. Chem.* **125**, 102 (2016).
  - [12] H. Küst and W. Mehlhorn, *J. Phys. B* **34**, 4155 (2001).
  - [13] M. Pauli, F. Rösel, and D. Trautmann, *J. Phys. B* **11**, 2511 (1978).
  - [14] F. Rösel, D. Trautmann, and G. Baur, *Z. Phys. A* **304**, 75 (1982).
  - [15] V. P. Petukhov, E. A. Romanovsky, N. M. Kabachnik, V. V. Sizov, and S. V. Ermakov, in *Proceedings of the 11th*

- International Conference on the Physics of Electronic and Atomic Collisions* (The Society for Atomic Collision Research, Japan, 1979), Vol. 1, p. 668.
- [16] A. Kumar, A. N. Agnihotri, S. Chatterjee, S. Kasthurirangan, D. Misra, R. K. Choudhury, L. Sarkadi, and L. C. Tribedi, *Phys. Rev. A* **81**, 062709 (2010).
- [17] D. H. Madison and E. Merzbacher, *Atomic Inner-Shell Processes* (Academic, New York, 1975).
- [18] D. Trautmann and F. Rösel, *Nucl. Instrum. Methods* **169**, 259 (1980).
- [19] M. S. Pindzola, *J. Phys. B* **48**, 015201 (2015).
- [20] X. Llovet, C. J. Powell, F. Salvat, and A. Jablonski, *J. Phys. Chem. Ref. Data* **43**, 013102 (2014).
- [21] L. C. Phinney, G. Lapicki, D. L. Weathers, F. U. Naab, J. L. Duggan, and F. D. McDaniel, *J. Phys. B* **45**, 035205 (2012).
- [22] T. E. I. Nassar, *Results Phys.* **17**, 103040 (2020).
- [23] M. Oswal, S. Kumar, U. Singh, S. Singh, G. Singh, K. P. Singh, D. Mehta, A. M. P. Mendez, D. M. Mitnik, C. C. Montanari, D. Mitra, and T. Nandi, *Radiat. Phys. Chem.* **176**, 108809 (2020).
- [24] S. Singh, S. Chatterjee, D. Mitra, and T. Nandi, *Measurement* **187**, 110322 (2022).
- [25] V. Jonauskas, *At. Data Nucl. Data Tables* **135–136**, 101363 (2020).
- [26] G. Purohit, *Nucl. Instrum. Meth. Phys. Res., Sect. B* **487**, 52 (2021).
- [27] R. D. Deslattes, E. G. Kessler, P. Indelicato, L. Billy, E. Lindroth, and J. Anton, *Rev. Mod. Phys.* **75**, 35 (2003).
- [28] <https://www.amptek.com>.
- [29] M. Terauchi, H. Takahashi, N. Handa, T. Murano, M. Koike, T. Kawachi, T. Imazono, N. Hasegawa, M. Koeda, T. Nagano, H. Sasai, Y. Oue, Z. Yonezawa, and S. Kuramoto, *Microscopy* **62**, 391 (2013).
- [30] F. Fernandez, A. Sepúlveda, J. Trincavelli, and G. Castellano, *Ultramicroscopy* **232**, 113401 (2022).
- [31] S. I. Salem, S. L. Panossian, and R. A. Krause, *At. Data Nucl. Data Tables* **14**, 91 (1974).
- [32] J. H. Scofield, *At. Data Nucl. Data Tables* **14**, 121 (1974).
- [33] V. Horvat, *Comput. Phys. Commun.* **180**, 995 (2009).
- [34] W. Bambynek, B. Crasemann, R. W. Fink, H. U. Freund, H. Mark, C. D. Swift, R. E. Price, and R. V. Rao, *Rev. Mod. Phys.* **44**, 716 (1972).
- [35] J. L. Campbell, *At. Data Nucl. Data Tables* **85**, 291 (2003).
- [36] J. Wigger, H. Altevogt, M. Brüssermann, G. Richter, and B. Cleff, *J. Phys. B* **17**, 4721 (1984).
- [37] X. Wang, Y. Zhao, R. Cheng, X. Zhou, G. Xu, Y. Sun, Y. Lei, Y. Wang, J. Ren, Y. Yu, Y. Li, X. Zhang, Y. Li, C. Liang, and G. Xiao, *Phys. Lett. A* **376**, 1197 (2012).